

## UC Davis

### UC Davis Previously Published Works

**Title**

New Means to Control Molecular Assembly

**Permalink**

<https://escholarship.org/uc/item/8vv370k8>

**Journal**

The Journal of Physical Chemistry C, 124(11)

**ISSN**

1932-7447

**Authors**

Zhang, Jiali

Yu, Hai

Harris, Bradley

et al.

**Publication Date**

2020-03-19

**DOI**

10.1021/acs.jpcc.9b11377

Peer reviewed

## C: Physical Processes in Nanomaterials and Nanostructures

**A New Means to Control Molecular Assembly**Jiali Zhang, Hai Yu, Bradley Harris, Yunbo Zheng, Umit Celik, Lan Na,  
Roland Faller, Xi Chen, Dominik R. Haudenschild, and Gang-yu Liu*J. Phys. Chem. C*, **Just Accepted Manuscript** • DOI: 10.1021/acs.jpcc.9b11377 • Publication Date (Web): 23 Feb 2020Downloaded from [pubs.acs.org](https://pubs.acs.org) on March 4, 2020**Just Accepted**

“Just Accepted” manuscripts have been peer-reviewed and accepted for publication. They are posted online prior to technical editing, formatting for publication and author proofing. The American Chemical Society provides “Just Accepted” as a service to the research community to expedite the dissemination of scientific material as soon as possible after acceptance. “Just Accepted” manuscripts appear in full in PDF format accompanied by an HTML abstract. “Just Accepted” manuscripts have been fully peer reviewed, but should not be considered the official version of record. They are citable by the Digital Object Identifier (DOI®). “Just Accepted” is an optional service offered to authors. Therefore, the “Just Accepted” Web site may not include all articles that will be published in the journal. After a manuscript is technically edited and formatted, it will be removed from the “Just Accepted” Web site and published as an ASAP article. Note that technical editing may introduce minor changes to the manuscript text and/or graphics which could affect content, and all legal disclaimers and ethical guidelines that apply to the journal pertain. ACS cannot be held responsible for errors or consequences arising from the use of information contained in these “Just Accepted” manuscripts.

# A New Means to Control Molecular Assembly

*Jiali Zhang,<sup>1</sup> Hai Yu,<sup>1</sup> Bradley Harris,<sup>2</sup> Yunbo Zheng,<sup>1</sup> Umit Celik,<sup>1</sup> Lan Na,<sup>1</sup> Roland Faller,<sup>2</sup> Xi Chen,<sup>1</sup> Dominik R Haudenschild,<sup>3</sup> Gang-yu Liu<sup>1\*</sup>*

<sup>1</sup> Department of Chemistry, University of California, Davis, California, 95616, United States

<sup>2</sup> Department of Chemical Engineering, University of California, Davis, California, 95616, United States

<sup>3</sup> Department of Orthopaedic Surgery, University of California, Davis Medical Center, Sacramento, California, 95817, United States

**\* author to whom correspondence should be addressed**

Gang-yu Liu, Ph.D.  
University of California, Davis  
Department of Chemistry  
Davis, CA 95616  
Phone : (530) 754-9678  
Fax : (530) 754-8557  
Email: [gylu@ucdavis.edu](mailto:gylu@ucdavis.edu)

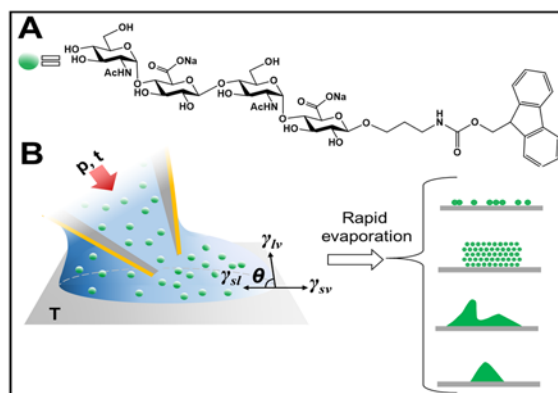
1  
2  
3 **ABSTRACT:** While self-assembly of molecules is relatively well-known and frequently utilized  
4  
5 in chemical synthesis and material science, controlled assembly of molecules represents a new  
6  
7 concept and approach. The present work demonstrates the concept of controlled molecular  
8  
9 assembly using a non-spherical biomolecule, heparosan tetrasaccharide (MW = 1.099 kD). The  
10  
11 key to controlled assembly is the fact that ultra-small solution droplets exhibit different  
12  
13 evaporation dynamics from those of larger ones. Using an independently controlled microfluidic  
14  
15 probe in an atomic force microscope, sub-femtoliter aqueous droplets containing designed  
16  
17 molecules produce well-defined features with dimensions as small as tens of nanometers. The  
18  
19 initial shape of the droplet and the concentration of solute within the droplet dictate the final  
20  
21 assembly of molecules due to the ultrafast evaporation rate and dynamic spatial confinement of  
22  
23 the droplets. The level of control demonstrated in this work brings us closer to programmable  
24  
25 synthesis for chemistry and materials science which can be used to develop vehicles for drug  
26  
27 delivery 3-D nanoprinting in additive manufacturing.  
28  
29  
30  
31  
32  
33  
34  
35  
36  
37  
38  
39  
40  
41  
42  
43  
44  
45  
46  
47  
48  
49  
50  
51  
52  
53  
54  
55  
56  
57  
58  
59  
60

## INTRODUCTION

Assembly of molecules into meso-scale structures by design still poses great challenges, despite pronounced advances in bottom-up and top-down approaches.<sup>1, 2</sup> Self-assembly (SA) provides a powerful means to address this challenge. Ordered structures driven by thermodynamics have been reported, including self-assembled monolayers (SAMs),<sup>3-5</sup> phase-separated polymers,<sup>6-9</sup> and lipid bilayers.<sup>10, 11</sup> In attempts to produce molecular assemblies by design, the concept of controlled assembly was demonstrated in our prior work via the formation of various assemblies of spherical macromolecules, such as star polymers (MW = 383 kD, Rh = 47 nm).<sup>12</sup> The key to controlled molecular assembly relies on an ultrafast evaporation rate and spatial confinement by small droplets (sub-fL), as illustrated in Figure 1. The rapid evaporation locks the solute molecules in place, leading to a high degree of control over the feature geometry and intra-feature molecular packing.<sup>12</sup> The dynamic confinement was controlled by the regulation of volume, and evaporation scenario such as constant contact area evaporation on solution-philic/hydrophilic surface<sup>12-15</sup> or constant contact angle evaporation on solution-phobic/hydrophobic surface.<sup>12, 13, 16-20</sup>

The present work pushes the concept of controlled assembly to smaller and non-spherical molecules, e.g., heparosan tetrasaccharide (referred to as heparosan, MW = 1.099 kD), as shown in Figure 1. Heparosan is a polysaccharide consisting of disaccharide repeat units of  $\alpha$ 1–4-linked *N*-acetyl-D-glucosamine (GlcNAc) and  $\beta$ 1–4-linked D-glucuronic acid (GlcA).<sup>21</sup> It is produced as a capsule polysaccharide (CPS) by both *P. multocida* Type D and *E. coli* K5.<sup>22</sup> It is also the polysaccharide backbone of heparin and heparan sulfate found in mammals.<sup>23</sup> Assemblies of heparosan, e.g. nanogels,<sup>24</sup> micelles,<sup>25-28</sup> and nanoparticles,<sup>29</sup> have been used for disease diagnosis and treatment. The formation of these molecular assemblies relies primarily on self-assembly.<sup>24-29</sup>

1  
2  
3 The size of such self-assembled units are typically in the range of 50-220 nm.<sup>24-29</sup> It was reported  
4 that particle size, size distribution, and morphology play important roles in their efficacy, as these  
5 factors impact cell-uptake and blood circulation time, as well as drug release.<sup>30</sup> Using various pre-  
6 designed ultrasmall droplets at defined solute concentration and initial droplet volume and  
7 geometry, this work demonstrates the feasibility for controlling molecular assembly of heparosan  
8 oligosaccharides. Specifically, the ability to control the assembly of heparosan nanostructures by  
9 design could significantly advance biomaterial development for drug delivery and theragnostic  
10 applications. In general, this level of control demonstrated in this work brings us closer to  
11 programmable synthesis for chemistry as well as developing vehicles for drug delivery and 3-D  
12 nanoprinting in additive manufacturing.  
13  
14  
15  
16  
17  
18  
19  
20  
21  
22  
23  
24  
25  
26



27  
28  
29  
30  
31  
32  
33  
34  
35  
36  
37  
38  
39  
40  
41 **Figure 1.** (A) Chemical structure of Fmoc-tagged heparosan tetrasaccharide. (B) A schematic  
42 diagram illustrating our concept of controlled assembly. An ultrasmall liquid droplet is delivered  
43 via a microfluidic probe to a surface with designed solvent-philicity. The droplet size and shape  
44 are dictated by the delivery parameters (e.g., p, t, T and probe location), and droplet-surface  
45 interactions ( $\theta$  and  $\gamma$  representing contact angle, and surface tensions at phase boundaries). The  
46 right column illustrates solute assemblies upon rapid solvent evaporation.  
47  
48  
49  
50  
51  
52  
53  
54  
55  
56  
57  
58  
59  
60

## EXPERIMENTAL METHODS

**Materials.** Glass slides with lateral dimensions of 75 mm × 25 mm and thicknesses of 1 mm were purchased from Fisher Scientific (Pittsburgh, PA). Glycerol (≥ 99%), sulfuric acid (95.0 – 98.0%), hydrogen peroxide (30% aqueous solution), and ammonium hydroxide (NH<sub>4</sub>OH, 30% aqueous solution) and toluene (99.8%) were purchased from Sigma-Aldrich (St. Louis, MO). *N*-(6-aminohexyl)-aminopropyltrimethoxysilane (AAPTMS) and octadecyltrichlorosilane (OTS) were purchased from Gelest (Morrisville, PA). Ethanol (99.5%) was purchased from KPTEC (King of Prussia, PA). Ultrapure water was attained from a Milli-Q water system with resistance of 18.2 MΩ·cm at 25 °C (EMD Millipore, Billerica, MA). Nitrogen gas (99.999%) was purchased from Praxair, Inc. (Danbury, CT, King of Prussia, PA). AC240TS-R3 silicon cantilevers were purchased from Oxford Instruments Asylum Research (Santa Barbara, CA). All other materials were used without further treatment or modification, unless otherwise stated.

Fmoc-tagged heparosan tetrasaccharide (referred to as “heparosan” hereafter) was chemoenzymatically synthesized from chemically synthesized Fmoc-tagged monosaccharide GlcAβProNHFmoc using a sequential one-pot multienzyme (OPME) process with alternating OPME GlcNAc-activation/transfer and OPME GlcA-activation/transfer systems.<sup>31</sup> Briefly, disaccharide GlcNAcα1–4GlcAβProNHFmoc was enzymatically synthesized from GlcAβProNHFmoc via a one-pot four-enzyme GlcNAc-activation and transfer system containing *B. longum* *N*-acetylhexosamine-1-kinase (BLNahK),<sup>32</sup> *P. multocida* *N*-acetylglucosamine-1-phosphate uridylyltransferase (PmGlmU),<sup>33</sup> *P. multocida* inorganic pyrophosphatase (PmPpA),<sup>34</sup> and Δ80PmHS2.<sup>31</sup> Trisaccharide GlcAβ1–4GlcNAcα1–4GlcAβProNHFmoc was then synthesized from the disaccharide using a one-pot four-enzyme GlcA-activation and transfer system containing *A. thaliana* glucuronokinase (AtGlcAK),<sup>35</sup> *B. longum* UDP-sugar pyrophosphorylase,<sup>36</sup> PmPpA,

1  
2  
3 and  $\Delta 80\text{PmHS2}$ . Finally, the heparosan tetrasaccharide was readily synthesized from the  
4 trisaccharide using the OPME GlcNAc-activation/transfer system containing BLNahk, PmGlmU,  
5 PmPpA, and  $\Delta 80\text{PmHS2}$ .<sup>31</sup>  
6  
7

8  
9  
10 **Preparation of Self-Assembled Monolayers.** The goal of this step is to prepare a set of surfaces  
11 with designated solution-philicity using self-assembled monolayers (SAMs) on glass surfaces.  
12 Glass slides were cleaned following previously reported protocols.<sup>37-43</sup> In brief, substrates were  
13 cleaned using piranha solution by immersion for 1 h, then rinsed with copious quantities of  
14 ultrapure water. Piranha solution is a mixture of sulfuric acid and hydrogen peroxide at a (v/v)  
15 ratio of 3:1. It is highly corrosive and should be handled carefully. Then, the cleaned glass  
16 substrates were immersed in a prepared basic bath at 70 °C for 1 h. Basic bath is prepared by  
17 mixing ammonium hydroxide, hydrogen peroxide, and water at a (v/v) ratio of 5:1:1. Finally,  
18 substrates were again rinsed with copious quantities of ultrapure water and dried in nitrogen gas.  
19 The hydrophilicity of glass substrates was modified using silane chemistry, following established  
20 protocols.<sup>37-43</sup> To modify glass slides with amine-terminated silane AAPTMS SAMs, the clean  
21 glass slides were placed into a sealed Teflon container (100 mL) containing 200  $\mu\text{L}$  of AAPTMS,  
22 then heated in an oven at 70 – 80 °C for 2 h. The substrate was then rinsed with ethanol and  
23 deionized water, sequentially, followed by drying in nitrogen gas. To prepare OTS-modified glass  
24 slides, freshly cleaned glass slides were immersed in a solution of 5 mM OTS in toluene for 30  
25 min, followed by rinsing with toluene and ethanol, and then dried in nitrogen gas.  
26  
27  
28  
29  
30  
31  
32  
33  
34  
35  
36  
37  
38  
39  
40  
41  
42  
43  
44  
45

46  
47 **Contact Angle Measurement.** Contact angle data were collected for the modified substrates with  
48 a VCA Optima Contact Angle Measurement system (AST Products, Billerica, MA), following  
49 standard protocols.<sup>12, 44-46</sup> A 3  $\mu\text{L}$  drop of designated solution was placed on surfaces using an  
50 Hamilton 700 series HPLC needle (Hamilton Co., Reno, Nev.). At least three different positions  
51  
52  
53  
54  
55  
56  
57

1  
2  
3 per sample were tested to assure reproducibility and accuracy. For solution of heparosan with  
4 concentration of  $2 \times 10^{-5}$  M in a mixed solvent of glycerol:H<sub>2</sub>O = 5:95 (v/v), the contact angle on  
5 AAPTMS SAM and OTS SAM was 59° and 107°, respectively. Reducing concentration to of  $2 \times$   
6  $10^{-6}$  M lead to 63 ° on AAPTMS SAM and 102 ° on OTS SAM. For  $2 \times 10^{-5}$  M aqueous solutions,  
7 the contact angle was measured to be 67° on AAPTMS SAM and 104° on OTS SAM, which are  
8 very similar to the contact angle of pure water on AAPTMS (58°)<sup>47, 48</sup> and OTS SAMs (110°)<sup>49, 50</sup>,  
9 respectively.  
10  
11  
12  
13  
14  
15  
16  
17  
18

19 **Microfluidic Delivery of Ultrasmall Liquid Droplets.** A state-of-the-art microfluidic system,  
20 FluidFM Bot,<sup>12, 51-54</sup> equipped with an independent hollow probe was used to dispense  
21 heparosan solution down to attoliter volume onto the designated surfaces. This system combines  
22 an AFM probe assembly, a precise x-y motorized stage, an inverted optical microscope and a  
23 pressure controller. The cantilever contains a microchannel and a reservoir and is connected to a  
24 pressure controller (-800 to 1000 mbar, 1 mbar precision) to dispense liquid inside the AFM head  
25 to guide the cantilever vertical movement. For optical view, an inverted microscope was used for  
26 imaging and facilitating stage control. A digital microscope was installed to monitor laser  
27 position and probe movement. Microchanneled hollow probes with 300 nm square aperture at  
28 apex of the tip were utilized. The hollow probe was prefilled with designed heparosan  
29 tetrasaccharide solution, with a square pyramidal tip tilting 11° from the surface normal. The  
30 cantilevers were made of Si. Initially, 1 μL of the designated heparosan tetrasaccharide solution  
31 was filled into the probe's 2 μL reservoir. The contact force or load was set to 80 nN for all  
32 delivery reported in this work.  
33  
34  
35  
36  
37  
38  
39  
40  
41  
42  
43  
44  
45  
46  
47  
48  
49  
50

51 **AFM Characterization of Heparosan Assemblies.** After droplet deposition, liquid evaporates  
52 rapidly as monitored via bright field optical microscopy. To avoid any residual solvent and  
53  
54  
55  
56  
57

1  
2  
3 facilitate atomic force microscopy (AFM) characterization, the glass slides were placed in a clean  
4 ambient environment overnight unless specified. The AFM (MFP-3D, Oxford Instrument, Santa  
5 Barbara, CA) has a deflection configuration. Silicon probes (AC 240-TS, Olympus America,  
6 Central Valley, PA) with a force constant of 1.7 N/m and resonance frequency of 70 kHz. Tapping  
7 mode was utilized for imaging with damping set at 40-60%. The AFM images were analyzed using  
8 the Asylum MFP-3D software developed on an Igor Pro 6.12 platform.  
9  
10  
11  
12  
13  
14  
15  
16  
17  
18

## 19 RESULTS AND DISCUSSION

20  
21  
22 **Controlling Molecular Packing.** Our previous work on the controlled assembly of star polymers  
23 demonstrated the packing can be controlled from random distribution to closely packed structure  
24 within monolayer-, bilayer- or multilayer-disks.<sup>12</sup> The disk geometry is primarily attributed to  
25 constant area evaporation of the droplets on solution-philic surfaces.<sup>12-15</sup> In contrast to star  
26 polymers which are almost rigid with spherical shape,<sup>12, 55</sup> individual heparosan molecules  
27 dissolved in aqueous solutions are flexible and linear, making them “semi-flexible rods”. The  
28 critical question is whether our approach enables control over the packing of heparosan. Figure 2A  
29 reveals a heparosan disk formed upon delivery and evaporation of a 2.56 pL droplet of  $2 \times 10^{-6}$  M  
30 heparosan tetrasaccharide solution onto a clean aminopropyltrimethoxysilane (AAPTMS) SAM  
31 surface. The AAPTMS SAM surface is solution-philic with a contact angle of  $63^\circ$ . Thus, the  
32 droplet appeared to spread. Upon evaporation, a disk was formed covering  $8.3 \mu\text{m}^2$  area, i.e. the  
33 interfacial area of the initial droplet on AAPTSM SAM surface. Within the disk, randomly  
34 distributed molecular clusters were clearly visible (bright features) in Figure 2B. These clusters  
35 are relatively homogeneous in size, 3.5-9.5 nm in height. These clusters are well separated, 40-220  
36 nm among the nearest neighbors (NN). Increasing amount of materials delivered, e.g. 4.36 pL  
37  
38  
39  
40  
41  
42  
43  
44  
45  
46  
47  
48  
49  
50  
51  
52  
53  
54  
55  
56  
57  
58  
59  
60

droplets, led to larger disks, for example, a  $11.2 \mu\text{m}^2$  area disk shown in Figure 2C. Within the disk, clusters of similar size to Figure 2B are also seen, as shown in Figure 2D. These clusters exhibit heights of 12-18 nm with NN separation 18-39 nm, i.e. similar in size but more closely packed than in Figure 2A. The formation of disk containing randomly distributed solute clusters is consistent with constant contact area evaporation.<sup>12-15</sup> The presence of clusters instead of individual heparosan molecules is attributed to molecular clustering during evaporation, based on our molecular dynamics (MD) simulation (see below). Increasing heparosan tetrasaccharide concentration and/or amount further decreases cluster separation. At  $2 \times 10^{-5}$  M and 0.833 pL, a heparosan disk was formed: 23.7 nm tall and  $5.414 \mu\text{m}$  wide, as shown in Figure 2E. Within the disk, clusters of heparosan are packed in an over-crowding way, as seen Figure 2F, manifesting to a smoother disk surface than lower coverage cases.

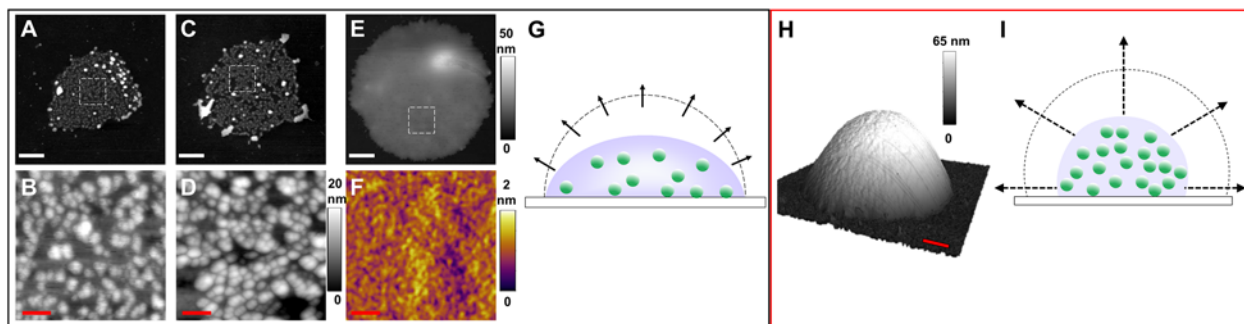
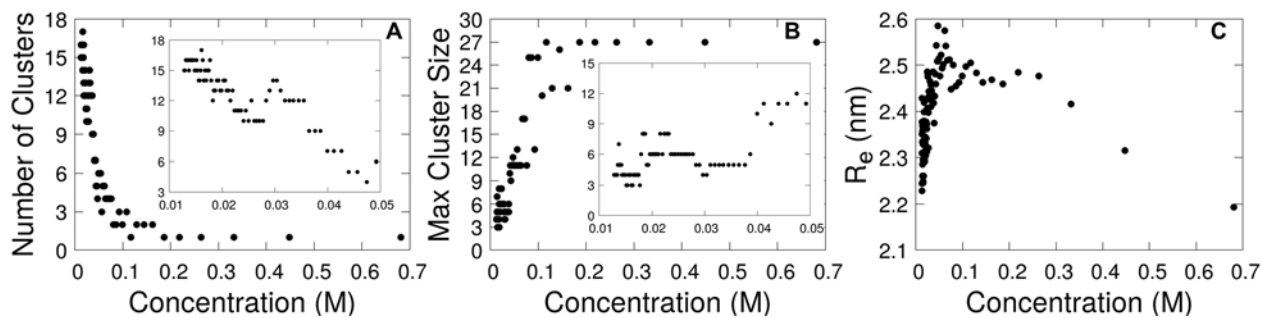


**Figure 2.** (A) Atomic force microscopy (AFM) topographic image of a disk of heparosan formed after delivery a droplet under 20 mbar for 4.02 s on AAPTMS/glass. Solution concentration:  $2 \times 10^{-6}$  M. (B) A zoomed-in view of the defined area (square frame) in (A). (C) Similar to (A) except with high pressure and longer deliver time, 100 mbar and 5 s, respectively. (D) A zoom-in image as defined in [C]. (E) Similar to (B) except higher concentration of heparosan,  $2 \times 10^{-5}$  M. (F) A zoom-in image of as defined in E (squared area). (G) Schematic diagram illustrates the constant contact area evaporation of a droplet on hydrophilic AAPTMS/glass surface. Broken

1  
2  
3 line and array arrows represent initial droplet boundary, and evaporation direction and rate,  
4  
5 respectively. (H) AFM topography of a mound formed on OTS/glass under the same delivery  
6  
7 condition as (E). (I) Schematic diagram illustrates the constant contact angle evaporation for  
8  
9 droplet on hydrophobic surface. The scale bars for white and red bars are 1  $\mu\text{m}$  and 200 nm,  
10  
11  
12 respectively.  
13  
14  
15

16 The molecular dynamics (MD) simulations (see details in Table S1) reveal a more  
17  
18 detailed molecular process during evaporation. Indeed, the outcomes show a progression of  
19  
20 heparosan from individual molecules in aqueous solution to aggregate, and then finally to a  
21  
22 polymer melt. This is best seen quantitatively in Figure 3, suggesting the solution phase is below  
23  
24 0.04 M, a transition phase between 0.04-0.1 M, and a transition towards a polymer melt  
25  
26 beginning at 0.3 M. While the actual concentration used in experiments is  $\mu\text{M}$ , the simulated  
27  
28 concentrations were much higher than those used experimentally in order to speed up the  
29  
30 aggregation trends to reasonable simulation times and to replicate the conditions of water  
31  
32 removal leading to sugar molecules packing together. For the y axis for Figure 3, a cluster is 1  
33  
34 or more sugar molecules within an angstrom of another sugar molecule. For Figure 3A this  
35  
36 means that individual sugars appear on the y-axis as a cluster, i.e. the maximum possible number  
37  
38 of clusters is 27. Figure 3A and 3B taken together provide insight on the relevant range of  
39  
40 concentrations for which aggregation begins. Insets in these Figures are included to differentiate  
41  
42 the concentrations and transition below 0.045 M. An understanding of what the sugars are doing  
43  
44 in these regions is best seen by the end-to-end distance in Figure 3C. At concentrations below  
45  
46 0.04 M, the sugars have favorable enough interactions with water that they remain flexible and  
47  
48 independent in solution. As the sugars are pushed together as concentration increases, the  
49  
50 individual sugar molecules extend to find each other in solution and increase favorable  
51  
52  
53  
54  
55  
56  
57  
58  
59  
60

1  
2  
3 interactions. This mechanism explains the presence of distributed aggregates or “clusters”  
4  
5 observed in the experimental disk features. The concentration range for this transition  
6  
7 corresponds to approximately 0.04- 0.1 M. The maximum end-to-end distance in this region  
8  
9 approximates the end-to-end distance obtained through ChemDraw (2.55 nm). This  
10  
11 concentration range corresponding to chain expansion correlates to a decrease in overall number  
12  
13 of clusters and an increase in maximum cluster size as shown in Figures 3A and 3B. Figures 4A-  
14  
15 4C provide a more direct visualization of the transition from individual molecules to a cluster in  
16  
17 the molecular dynamics simulations, as this can be useful insight into the locations aggregation  
18  
19 sites occur. Additional simulation analysis for this transition behavior is presented in Figures  
20  
21 sites occur. Additional simulation analysis for this transition behavior is presented in Figures  
22  
23 S1-S2 of Support Information (SI).  
24  
25  
26



27  
28  
29  
30  
31  
32  
33  
34  
35  
36  
37  
38 **Figure 3.** (A) Number of heparosan clusters during each simulation. Inlay is below 0.045 M (B)  
39  
40 Maximum number of heparosan in a cluster at any given state during simulations during  
41  
42 evaporation. Inlay is below 0.045 M. (C) The average end to end distance of the heparosan during  
43  
44 each simulation.  
45  
46  
47  
48  
49  
50  
51  
52  
53  
54  
55  
56  
57  
58  
59  
60

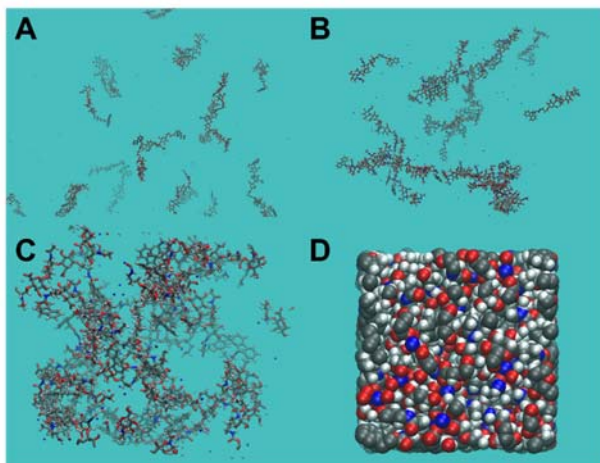


**Figure 4.** A ball-and-stick model displaying the molecular states from our MD simulation at (A) 0.0138 M, in a  $15 \times 15 \times 15 \text{ nm}^3$  box; (B) 0.049 M in a  $9.4 \times 9.4 \times 9.4 \text{ nm}^3$  box; and (C) 0.218 M in a  $4.0 \times 4.0 \times 4.0 \text{ nm}^3$  box. (D) Volume filling model from our MD simulation at 1.3 M in a  $3.2 \times 3.2 \times 3.2 \text{ nm}^3$  box.

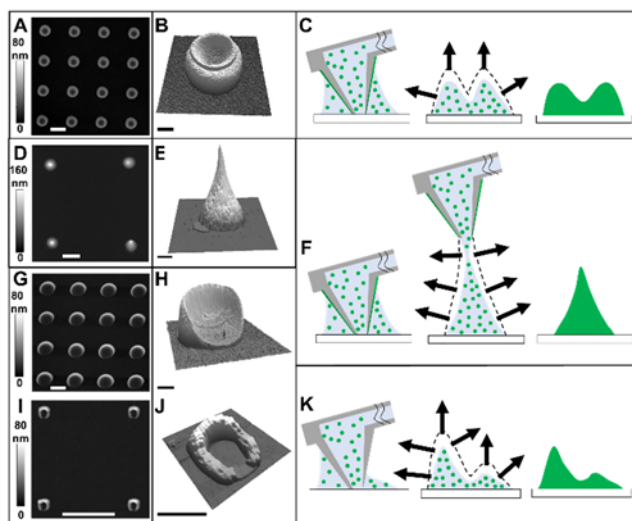
In our attempt to further increase molecular packing and form a mound geometry, constant contact angle evaporation was adopted.<sup>12, 13, 16-20</sup> In this case, droplets of heparosan tetrasaccharide solution were delivered onto octadecyltrichlorosilane (OTS) SAM surfaces. The contact angle of the heparosan solution measured  $107^\circ$ , thus the droplets maintained a spherical hat geometry throughout evaporation. Evaporation of 0.113 pL of  $2 \times 10^{-5}$  M heparosan solution led to mound formation, as shown in Figure 2H. The mound is  $1.779 \mu\text{m}$  wide at the base and  $111.7 \text{ nm}$  tall. The exterior of the mound appeared homogenous, as revealed in Figure 2H. In other words, the clusters collapsed and merged to form a single assembly. Given the spatial confinement and rapid evaporation, heparosan molecules were closely jammed within each assembly, analogous to the interdigitated state of chains among star polymers in a mound.<sup>12</sup> This approach enables control over the size of each mound (or number of molecules in a single assembly), by varying the heparosan concentration and droplet volume.

1  
2  
3 Our MD simulations rationalize the transition from aggregates to this polymer-melt-like state. At  
4 concentrations above 0.3 M, corresponding to the final 4% of water molecules, a transition to the  
5 melt-like state is observed. The removal of the final few percents of water corresponds to a melt-  
6 like transition shown in Figure 3C. The end-to-end distance drops from the elongated molecules  
7 observed in the transitional and aggregate state. Under spatial confined situation, such as the  
8 constant-contact-angle evaporation, the molecules begin to follow a random walk as all  
9 interactions become equal among the other heparosan, compared to the self-avoiding walk the  
10 heparosan molecules experienced with competing interactions between the heparosan and water.  
11 Figure 4D shows a visualization of this state in the simulation.  
12  
13  
14  
15  
16  
17  
18  
19  
20  
21  
22  
23  
24

25 Control over the Geometry of Individual Features. As discussed in the introduction, ultra-small  
26 droplet size and rapid evaporation are key to achieving controlled molecular assembly. While  
27 previous sections addressed the molecular packing within each feature upon initial delivery of  
28 spherical hat shaped droplets, this section reports non-spherical hat shaped droplets, leading to  
29 assemblies of solutes in more complex geometries than simple disks or mounds.  
30  
31  
32  
33  
34  
35  
36

37 Figure 5A shows  $4 \times 4$  arrays of “volcano-like” features. Each feature was produced by dispensing  
38 154 fL of  $2 \times 10^{-5}$  M heparosan tetrasaccharide solution onto an AAPTMS SAM covered glass  
39 surface. The delivery conditions:  $t = 1$  s,  $p = 100$  mbar with a contact force of 80 nN. Individual  
40 features can be clearly visualized as shown in Figure 5B: base diameter of 1.95-2.33  $\mu\text{m}$  and with  
41 the volcanic height of 23.9-31.5 nm. The top opening measures 0.95-1.25  $\mu\text{m}$  wide and 5.6-11 nm  
42 deep. The formation of this geometry is illustrated in Figure 5C. The exterior of the tip apex was  
43 pre-treated by dipping it into the solution and then letting it dry. Thus, the exterior of the tip apex  
44 becomes very solution-philic, leading to symmetric climbing of liquid during delivery via capillary  
45 interactions. The evaporation is faster than that seen in Figure 2 because the solvent here is pure  
46  
47  
48  
49  
50  
51  
52  
53  
54  
55  
56  
57  
58  
59  
60

1  
2  
3 water. Therefore, the final assembly adopts a similar geometry to the initial droplet. The upper  
4  
5 “lip” was likely formed during the final separation of the tip from the droplet, when the residual  
6  
7 amount of liquid fell atop of the partially evaporated droplet. The result shown in Figure 5A is  
8  
9 reproducible and robust, as taller volcanos were produced by increasing the amount of material  
10  
11 delivered, e.g., taller volcanos than the one in Figure 5A were produced (height = 42.4-87.1 nm)  
12  
13 by increasing injection time from 1 to 3 s under delivery pressure of 400 mbar (more detailed  
14  
15 outputs are included in Figure S3 and Table S2 in SI).  
16  
17  
18  
19



20  
21  
22  
23  
24  
25  
26  
27  
28  
29  
30  
31  
32  
33  
34  
35  
36  
37  
38 **Figure 5.** (A) An AFM topographic image of a 4x4 array of heparosan assemblies exhibiting  
39  
40 volcano-like shape. (B) A 3-D display of a single feature from (A) revealing clearly the volcano-  
41  
42 shaped geometry. (C) Schematic diagram illustrating characteristic moment of controlled  
43  
44 assembly: during dispensing, immediately after probe withdrawal, and final assembly after solvent  
45  
46 evaporation. Constant contact area evaporation occurred. The broken line and array arrows  
47  
48 represent initial droplet boundary, and evaporation direction and rate, respectively. (D) AFM  
49  
50 topographic image of a 2x2 array of heparosan assemblies with teepee-like shape. (E) A 3-D  
51  
52 display of a single feature from (D) revealing clearly the teepee geometry. (F) Schematic diagram  
53  
54  
55  
56  
57  
58  
59  
60

1  
2  
3 illustrating the assembly leading to teepee shape geometry. (G) AFM topographic image of a 4×4  
4 array of heparosan assemblies exhibiting asymmetry. (H) A 3-D display of a single feature from  
5  
6 (G) clearly revealing the bean-bag geometry. (K) Schematic diagram illustrates the assembly  
7  
8 leading to asymmetric geometry. (I) AFM topographic image of a 2×2 array of heparosan  
9  
10 assemblies exhibiting asymmetry. (J) A 3-D display of a single feature from (I). Scale bars are  
11  
12 2500 nm and 500 nm for white and black bars, separately. Z-scale in the 3-D displays is  
13  
14 exaggerated to allow clear visualization of the feature geometry.  
15  
16  
17  
18  
19

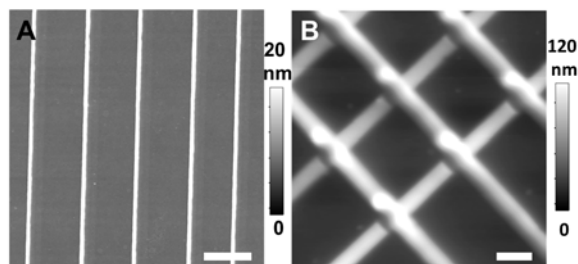
20  
21 The proposed mechanism is further validated by forming “teepee” features, a 2x2 array  
22 shown in Figures 5D, under identical conditions except using a mixed solvent of glycerol:H<sub>2</sub>O =  
23 5:95 (v/v) and lower concentration of  $2 \times 10^{-6}$  M. Adding the small amount (5%) of glycerol slowed  
24  
25 down the evaporation, allowing the solvent to merge and form capillary neck upon retreat of the  
26  
27 tip, as illustrated in Figure 5F. The sharp tent top, clearly visible in Figure 5E, is due to the capillary  
28  
29 neck formed at the final withdrawal. Further addition of glycerol could increase stickiness and  
30  
31 viscosity of the solution, leading to the sharper and longer tent top, as illustrate in Figure 5F. The  
32  
33 features in Figures 5D have a base diameter of 2.07-2.29  $\mu\text{m}$ , and a height of 140-180 nm. The  
34  
35 results were reproducible and robust. Under the same dwelling time of 0.5 s, increasing injection  
36  
37 pressure from 500 to 900 mbar leads to increased teepee base (from 1.20 to 2.02  $\mu\text{m}$ ), and height  
38  
39 (from 54 to 165 nm).  
40  
41  
42  
43  
44  
45

46  
47 Without pre-treatment of the tip, asymmetric features, such as “bean-bag”, were formed as shown  
48  
49 in Figure 5G (a 4x4 array). The concentration of heparosan was  $2 \times 10^{-5}$  M in pure water. At  
50  
51 dwelling time of 1 s and injection pressure of 100 mbar, 176 fL of solution was delivered onto a  
52  
53 clean and hydrophilic AAPTMS glass. As clearly shown in Figure 5H, the bean-bag measures  
54  
55 2.42-2.8  $\mu\text{m}$  at base diameter, with high and low edges of 45.4-52.4 and 3.3-6.1 nm, respectively.  
56  
57  
58  
59  
60

1  
2  
3 We were able to tune the size of the beanbag by varying the amount of material delivered. The  
4 formation of these asymmetric geometries are illustrated in Figure 5K. In contrast to Figure 5C,  
5 the droplet did not exhibit significant climbing up the apex exterior surfaces, instead it adopts a  
6 geometry guided by the local contact angle, as shown in Figure 5K. Since the probe tilted  $11^\circ$  from  
7 the surface normal, the droplet adopted an asymmetric geometry. With the fast evaporation of  
8 water, the initial droplet shape dictated the final assembly of the solutes, leading to the bean-bag  
9 shaped features. Reducing the amount of material, further lowering the symmetry, as shown in  
10 Figure 5I, a 4x4 array of “horseshoe” features was formed. Each feature represents a heparosan  
11 assembly, after dispensing 78.4 aL of 0.01 M heparosan aqueous solution on to the surfaces and  
12 drying. The horseshoe geometry is clearly visible in Figure. 5J, with the maximum height of 95.7  
13 nm. The full width at half maximum (FWHM) for both sides measure 137-153 and 143-161 nm  
14 with a separation of 307-359 nm. These results, collectively, demonstrate the high degree of control  
15 over the geometry of the molecular assembly by controlling the initial droplet geometry. Being  
16 stored in a clean environment under ambient conditions, these heparosan structures are stable  
17 beyond 4 months, based on time-dependent AFM imaging.

18  
19  
20  
21  
22  
23  
24  
25  
26  
27  
28  
29  
30  
31  
32  
33  
34  
35  
36  
37  
38  
39 **Applying Controlled Molecular Assembly to Enable 3-D Nanoprinting.** With the knowledge  
40 gained above, i.e. control the assembly of heparosan via controlling the droplets dispensed, 3-D  
41 nanoprinting shall be achievable by continuous delivery of solutions following the designed  
42 trajectory. The key is maintaining consistent and homogenous assembly of heparosan throughout  
43 the printing process. In other words, the controlled molecular assembly must be maintained at each  
44 transient spot of printing. Figure 6A demonstrates that lines of heparosan can be printed.  
45 Heparosan solution ( $2 \times 10^{-5}$  M) was delivered continuously on an AAPTMS/Si surface under  $p =$   
46 100 mbar, at a speed of  $10 \mu\text{m/s}$ . Under the delivery conditions, the transient time at each point is  
47  
48  
49  
50  
51  
52  
53  
54  
55  
56  
57  
58  
59  
60

1  
2  
3 equivalent to a droplet deposition with dwell time of 0.4 s. Therefore, after solvent evaporation,  
4  
5 the heparosan assembled into continuous lines with high degree of consistency and homogeneity.  
6  
7 All 25 lines are 50  $\mu\text{m}$  long, 116 nm wide and 26 nm tall, 5 of which are as shown in Figure 6A.  
8  
9 The separation among the lines shown in Figure 6A measures 2.15, 2.09, 2.18 and 1.87  $\mu\text{m}$ ,  
10  
11 respectively, from right to left. The reproducibility was demonstrated by repeating the identical  
12  
13 printing arrays of lines with the same geometries and size. The homogeneity and the size of the  
14  
15 printing arrays of lines with the same geometries and size. The homogeneity and the size of the  
16  
17 lines is consistent with the mechanism: at each point of delivery, constant area evaporation occur  
18  
19 rapidly analogous to that in Figure 2G. The line width is tunable by the concentration and speed,  
20  
21 e.g. slower speed leads to wider lines.  
22  
23  
24



25  
26  
27  
28  
29  
30  
31  
32  
33  
34  
35 **Figure 6.** (A) A 15  $\mu\text{m}$  x 15  $\mu\text{m}$  AFM topographic image of an array of heparosan lines. (B) A 15  
36  
37  $\mu\text{m}$  x 15  $\mu\text{m}$  AFM topographic image of stacking grids consisting of heparosan. Scale bars are 2  
38  
39  $\mu\text{m}$ .  
40  
41  
42

43  
44 Stacking grids, each layer perpendicular to another, were also printed under 200 mbar pressure,  
45  
46 and at 2  $\mu\text{m}/\text{s}$  speed. The grids covered a 15  $\mu\text{m}$  x 15  $\mu\text{m}$  area, with a portion shown in the AFM  
47  
48 image in Figure 6B. Each line 39-57 nm tall and 1.01-1.09  $\mu\text{m}$  wide, with periodicity or separation  
49  
50 of 5  $\mu\text{m}$ . The height of the cross section was measured to be 55-69 nm tall. The angle between top  
51  
52 and bottom line arrays are 90.0°. The high fidelity following the design demonstrates the feasibility  
53  
54 for 3-D nanoprinting using functional molecules such as heparosan.  
55  
56  
57

## CONCLUSIONS

Using heparosan tetrasaccharide as the functional solute, this work demonstrates our new concept of controlled assembly of molecules. The key to controlled assembly is the fact that ultra-small solution droplets follow different evaporation dynamics from those of larger ones. The initial shape of the droplet and the concentration of solute within the droplet dictate the evaporation mechanism and the final assembly of molecules due to the ultrafast evaporation rate and dynamic spatial confinement of the droplets. The level of control demonstrated in this work brings us closer to programmable synthesis and assembly for chemistry and materials science. Work is in progress to investigate temperature dependence of delivery, evaporation, and the assembly behavior. Future work also includes exploring its application in production of drug delivery vehicles, and 3-D nanoprinting in additive manufacturing.

## ASSOCIATED CONTENT

### Supporting Information (SI).

Molecular dynamics simulation details and additional analysis; and experimental robustness.

This following files are available free of charge.

Main supporting information file: Controlled assembly SI.doc

myffnonbonded.itp molecular dynamics forcefield for Fmoc-Heparosan Tetrasaccharide using itp file type.

### Notes

The authors declare no competing financial interest.

## ACKNOWLEDGMENTS

We thank Drs. Pablo Dörig, Dario Ossola at Cytosurge, Glattbrugg, Switzerland for helpful scientific discussion, and Ms. Susan Stagner for careful proof-reading. This work is supported by Gordon and Betty Moore Foundation, the National Science Foundation (CHE-1808829), Lawrence Livermore National Laboratory LDRD project 19-ERD-012, under department of Energy Contract DE-AC52-07NA27344, UC Davis and the National Institutes of Health (NIH) Common Fund Glycoscience Program grant, U01GM125288, and 1R01AR070239 - 01A1.

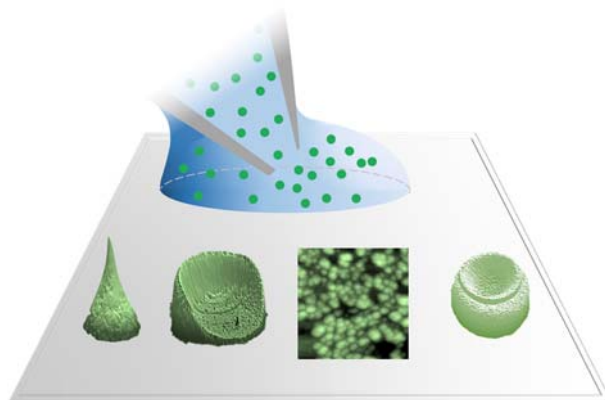
## REFERENCES

1. Whitesides, G. M.; Grzybowski, B., Self-assembly at all scales. *Science* **2002**, 295, (5564), 2418-2421.
2. Xia, Y.; Whitesides, G. M., Soft lithography. *Annual review of materials science* **1998**, 28, (1), 153-184.
3. Bain, C. D.; Troughton, E. B.; Tao, Y. T.; Evall, J.; Whitesides, G. M.; Nuzzo, R. G., Formation of monolayer films by the spontaneous assembly of organic thiols from solution onto gold. *Journal of the American Chemical Society* **1989**, 111, (1), 321-335.
4. Sagiv, J., Organized monolayers by adsorption. 1. Formation and structure of oleophobic mixed monolayers on solid surfaces. *Journal of the American Chemical Society* **1980**, 102, (1), 92-98.
5. Nuzzo, R. G.; Allara, D. L., Adsorption of bifunctional organic disulfides on gold surfaces. *Journal of the American Chemical Society* **1983**, 105, (13), 4481-4483.
6. Hillmyer, M. A.; Bates, F. S.; Almdal, K.; Mortensen, K.; Ryan, A. J.; Fairclough, J. P. A., Complex phase behavior in solvent-free nonionic surfactants. *Science* **1996**, 271, (5251), 976-978.
7. Hayward, R. C.; Pochan, D. J., Tailored Assemblies of Block Copolymers in Solution: It Is All about the Process. *Macromolecules* **2010**, 43, (8), 3577-3584.
8. Pochan, D. J.; Chen, Z. Y.; Cui, H. G.; Hales, K.; Qi, K.; Wooley, K. L., Toroidal triblock copolymer assemblies. *Science* **2004**, 306, (5693), 94-97.
9. Bigioni, T. P.; Lin, X. M.; Nguyen, T. T.; Corwin, E. I.; Witten, T. A.; Jaeger, H. M., Kinetically driven self assembly of highly ordered nanoparticle monolayers. *Nature Materials* **2006**, 5, (4), 265-270.
10. Nagle, J. F.; Tristram-Nagle, S., Structure of lipid bilayers. *Biochimica Et Biophysica Acta-Reviews on Biomembranes* **2000**, 1469, (3), 159-195.
11. Groves, J. T.; Ulman, N.; Boxer, S. G., Micropatterning fluid lipid bilayers on solid supports. *Science* **1997**, 275, (5300), 651-653.
12. Zhang, J.; Piunova, V. A.; Liu, Y.; Tek, A.; Yang, Q.; Frommer, J.; Liu, G.-y.; Sly, J., Controlled Molecular Assembly via Dynamic Confinement of Solvent. *The Journal of Physical Chemistry Letters* **2018**, 9, (21), 6232-6237.
13. Chhasatia, V. H.; Sun, Y., Interaction of bi-dispersed particles with contact line in an evaporating colloidal drop. *Soft Matter* **2011**, 7, (21), 10135-10143.
14. Ko, H.-Y.; Park, J.; Shin, H.; Moon, J., Rapid Self-Assembly of Monodisperse Colloidal Spheres in an Ink-Jet Printed Droplet. *Chemistry of Materials* **2004**, 16, (22), 4212-4215.
15. Park, J.; Moon, J., Control of colloidal particle deposit patterns within picoliter droplets ejected by ink-jet printing. *Langmuir* **2006**, 22, (8), 3506-3513.
16. Erbil, H. Y.; McHale, G.; Newton, M., Drop evaporation on solid surfaces: constant contact angle mode. *Langmuir* **2002**, 18, (7), 2636-2641.
17. Kuang, M.; Wang, J.; Bao, B.; Li, F.; Wang, L.; Jiang, L.; Song, Y., Inkjet Printing Patterned Photonic Crystal Domes for Wide Viewing-Angle Displays by Controlling the Sliding Three Phase Contact Line. *Advanced Optical Materials* **2014**, 2, (1), 34-38.
18. Kuncicky, D. M.; Velev, O. D., Surface-guided templating of particle assemblies inside drying sessile droplets. *Langmuir* **2008**, 24, (4), 1371-1380.
19. Picknett, R.; Bexon, R., The evaporation of sessile or pendant drops in still air. *J. Colloid Interface Sci* **1977**, 61, (2), 336-350.
20. Zhong, X.; Crivoi, A.; Duan, F., Sessile nanofluid droplet drying. *Adv. Colloid Interface Sci.* **2015**, 217, 13-30.
21. Wang, Z.; Dordick, J. S.; Linhardt, R. J., Escherichia coli K5 heparosan fermentation and improvement by genetic engineering. *Bioeng Bugs* **2011**, 2, (1), 63-67.

- 1  
2  
3  
4  
5  
6  
7  
8  
9  
10  
11  
12  
13  
14  
15  
16  
17  
18  
19  
20  
21  
22  
23  
24  
25  
26  
27  
28  
29  
30  
31  
32  
33  
34  
35  
36  
37  
38  
39  
40  
41  
42  
43  
44  
45  
46  
47  
48  
49  
50  
51  
52  
53  
54  
55  
56  
57  
58  
59  
60
22. DeAngelis, P. L.; Gunay, N. S.; Toida, T.; Mao, W. J.; Linhardt, R. J., Identification of the capsular polysaccharides of Type D and F *Pasteurella multocida* as unmodified heparin and chondroitin, respectively. *Carbohydrate research* **2002**, 337, (17), 1547-52.
  23. Sismey-Ragatz, A. E.; Green, D. E.; Otto, N. J.; Rejzek, M.; Field, R. A.; DeAngelis, P. L., Chemoenzymatic synthesis with distinct *Pasteurella* heparosan synthases: monodisperse polymers and unnatural structures. *The Journal of biological chemistry* **2007**, 282, (39), 28321-7.
  24. Rippe, M.; Stefanello, T. F.; Kaplum, V.; Britta, E. A.; Garcia, F. P.; Poirot, R.; Companhia, M. V. P.; Nakamura, C. V.; Szarpak-Jankowska, A.; Auzely-Velty, R., Heparosan as a potential alternative to hyaluronic acid for the design of biopolymer-based nanovectors for anticancer therapy. *Biomaterials science* **2019**, 7, (7), 2850-2860.
  25. Chen, J.-X.; Zhang, M.; Liu, W.; Lu, G.-Z.; Chen, J.-H., Construction of serum resistant micelles based on heparosan for targeted cancer therapy. *Carbohydrate Polymers* **2014**, 110, 135-141.
  26. Qiu, L.; Shan, X.; Long, M.; Ahmed, K. S.; Zhao, L.; Mao, J.; Zhang, H.; Sun, C.; You, C.; Lv, G.; Chen, J., Elucidation of cellular uptake and intracellular trafficking of heparosan polysaccharide-based micelles in various cancer cells. *International journal of biological macromolecules* **2019**, 130, 755-764.
  27. Sun, C.; Li, X.; Du, X.; Wang, T., Redox-responsive micelles for triggered drug delivery and effective laryngopharyngeal cancer therapy. *International journal of biological macromolecules* **2018**, 112, 65-73.
  28. Qiu, L.; Ge, L.; Long, M.; Mao, J.; Ahmed, K. S.; Shan, X.; Zhang, H.; Qin, L.; Lv, G.; Chen, J., Redox-responsive biocompatible nanocarriers based on novel heparosan polysaccharides for intracellular anticancer drug delivery. *Asian Journal of Pharmaceutical Sciences* **2018**.
  29. Chen, J.-X.; Liu, W.; Zhang, M.; Chen, J.-H., Heparosan based negatively charged nanocarrier for rapid intracellular drug delivery. *International Journal of Pharmaceutics* **2014**, 473, (1), 493-500.
  30. Danaei, M.; Dehghankhold, M.; Ataie, S.; Hasanzadeh Davarani, F.; Javanmard, R.; Dokhani, A.; Khorasani, S.; Mozafari, M. J. P., Impact of particle size and polydispersity index on the clinical applications of lipidic nanocarrier systems. **2018**, 10, (2), 57.
  31. Lan, N.; Ghosh, T.; McArthur, J. B.; Asbell, T.; Chen, X., Engineered *P. multocida* heparosan synthases improve size-controlled enzymatic synthesis of longer heparosan oligosaccharides. In *The Journal of the American Chemical Society*, 2019 (Submitted).
  32. Li, Y.; Yu, H.; Chen, Y.; Lau, K.; Cai, L.; Cao, H.; Tiwari, V. K.; Qu, J.; Thon, V.; Wang, P. G.; Chen, X., Substrate promiscuity of N-acetylhexosamine 1-kinases. *Molecules* **2011**, 16, (8), 6396-407.
  33. Chen, Y.; Thon, V.; Li, Y.; Yu, H.; Ding, L.; Lau, K.; Qu, J.; Hie, L.; Chen, X., One-pot three-enzyme synthesis of UDP-GlcNAc derivatives. *Chem Commun (Camb)* **2011**, 47, (38), 10815-7.
  34. Lau, K.; Thon, V.; Yu, H.; Ding, L.; Chen, Y.; Muthana, M. M.; Wong, D.; Huang, R.; Chen, X., Highly efficient chemoenzymatic synthesis of beta1-4-linked galactosides with promiscuous bacterial beta1-4-galactosyltransferases. *Chem Commun (Camb)* **2010**, 46, (33), 6066-8.
  35. Muthana, M. M.; Qu, J.; Xue, M.; Klyuchnik, T.; Siu, A.; Li, Y.; Zhang, L.; Yu, H.; Li, L.; Wang, P. G.; Chen, X., Improved one-pot multienzyme (OPME) systems for synthesizing UDP-uronic acids and glucuronides. *Chem Commun (Camb)* **2015**, 51, (22), 4595-8.
  36. Muthana, M. M.; Qu, J.; Li, Y.; Zhang, L.; Yu, H.; Ding, L.; Malekan, H.; Chen, X., Efficient one-pot multienzyme synthesis of UDP-sugars using a promiscuous UDP-sugar pyrophosphorylase from *Bifidobacterium longum* (BLUSP). *Chem Commun (Camb)* **2012**, 48, (21), 2728-30.
  37. Li, J. R.; Lusker, K. L.; Yu, J. J.; Garno, J. C., Engineering the spatial selectivity of surfaces at the nanoscale using particle lithography combined with vapor deposition of organosilanes. *ACS Nano* **2009**, 3, (7), 2023-2035.
  38. Li, J. R.; Garno, J. C., Elucidating the role of surface hydrolysis in preparing organosilane nanostructures via particle lithography. *Nano Letters* **2008**, 8, (7), 1916-1922.
  39. Lin, W. F.; Swartz, L. A.; Li, J. R.; Liu, Y.; Liu, G. Y., Particle Lithography Enables Fabrication of Multicomponent Nanostructures. *The Journal of Physical Chemistry C* **2013**, 117, (44), 23279-23285.

- 1  
2  
3  
4  
5  
6  
7  
8  
9  
10  
11  
12  
13  
14  
15  
16  
17  
18  
19  
20  
21  
22  
23  
24  
25  
26  
27  
28  
29  
30  
31  
32  
33  
34  
35  
36  
37  
38  
39  
40  
41  
42  
43  
44  
45  
46  
47  
48  
49  
50  
51  
52  
53  
54  
55  
56  
57  
58  
59  
60
40. Lin, W. F.; Li, J. R.; Liu, G. Y., Near-Field Scanning Optical Microscopy Enables Direct Observation of Moire Effects at the Nanometer Scale. *Acs Nano* **2012**, 6, (10), 9141-9149.
  41. Garno, J. C.; Batteas, J. D., Nanofabrication with self-assembled monolayers by scanning probe lithography. In *Applied Scanning Probe Methods IV: Industrial Applications*, **2006**; pp 105-135.
  42. Tian, T.; LeJeune, Z. M.; Serem, W. K.; Yu, J. J.; Garno, J. C., Nanografting: A method for bottom-up fabrication of designed nanostructures. In *Tip-Based Nanofabrication: Fundamentals and Applications*, 2011; pp 167-205.
  43. Lifang Shi, A. K., Jianli Zhao, Miquel Salmeron, Gang Yu Liu, High-Resolution Imaging of Cells Using Current Sensing Atomic Force Microscopy. *Lett. Appl. NanoBioScience* **2015**, 4, (4), 316-320.
  44. Abbott, N. L.; Gorman, C. B.; Whitesides, G. M., Active control of wetting using applied electrical potentials and self-assembled monolayers. *Langmuir* **1995**, 11, (1), 16-18.
  45. Bain, C. D.; Whitesides, G. M., A study by contact angle of the acid-base behavior of monolayers containing omega.-mercaptocarboxylic acids adsorbed on gold: an example of reactive spreading. *Langmuir* **1989**, 5, (6), 1370-1378.
  46. Yuan, W.; Van Ooij, W., Characterization of organofunctional silane films on zinc substrates. *Journal of Colloid Interface Science* **1997**, 185, (1), 197-209.
  47. Sugimura, H.; Hayashi, K.; Saito, N.; Nakagiri, N.; Takai, O., Surface potential microscopy for organized molecular systems. *Applied Surface Science* **2002**, 188, (3-4), 403-410.
  48. Hayashi, K.; Saito, N.; Sugimura, H.; Takai, O.; Nakagiri, N., Surface potential contrasts between silicon surfaces covered and uncovered with an organosilane self-assembled monolayer. *Ultramicroscopy* **2002**, 91, (1-4), 151-156.
  49. Mirji, S., Octadecyltrichlorosilane adsorption kinetics on Si (100)/SiO<sub>2</sub> surface: contact angle, AFM, FTIR and XPS analysis. *Surface Interface Analysis: An International Journal devoted to the development application of techniques for the analysis of surfaces, interfaces thin films* **2006**, 38, (3), 158-165.
  50. Wang, Y.; Lieberman, M., Growth of ultrasmooth octadecyltrichlorosilane self-assembled monolayers on SiO<sub>2</sub>. *Langmuir* **2003**, 19, (4), 1159-1167.
  51. Ventrici de Souza, J.; Liu, Y.; Wang, S.; Dörig, P.; Kuhl, T. L.; Frommer, J.; Liu, G.-y., Three-dimensional nanoprinting via direct delivery. *The Journal of Physical Chemistry B* **2017**, 122, (2), 956-962.
  52. Deng, W. N.; Wang, S.; Ventrici de Souza, J.; Kuhl, T. L.; Liu, G.-y., New Algorithm to Enable Construction and Display of 3D Structures from Scanning Probe Microscopy Images Acquired Layer-by-Layer. *The Journal of Physical Chemistry A* **2018**, 122, (26), 5756-5763.
  53. Meister, A.; Gabi, M.; Behr, P.; Studer, P.; Vörös, J. n.; Niedermann, P.; Bitterli, J.; Polesel-Maris, J.; Liley, M.; Heinzelmann, H., FluidFM: combining atomic force microscopy and nanofluidics in a universal liquid delivery system for single cell applications and beyond. *Nano letters* **2009**, 9, (6), 2501-2507.
  54. Grüter, R. R.; Vörös, J.; Zambelli, T., FluidFM as a lithography tool in liquid: spatially controlled deposition of fluorescent nanoparticles. *Nanoscale* **2013**, 5, (3), 1097-1104.
  55. Lee, V. Y.; Havenstrite, K.; Tjio, M.; McNeil, M.; Blau, H. M.; Miller, R. D.; Sly, J. J. A. M., Nanogel Star Polymer Architectures: A Nanoparticle Platform for Modular Programmable Macromolecular Self-Assembly, Intercellular Transport, and Dual-Mode Cargo Delivery. **2011**, 23, (39), 4509-4515.

TOC GRAPHIC



1  
2  
3  
4  
5  
6  
7  
8  
9  
10  
11  
12  
13  
14  
15  
16  
17  
18  
19  
20  
21  
22  
23  
24  
25  
26  
27  
28  
29  
30  
31  
32  
33  
34  
35  
36  
37  
38  
39  
40  
41  
42  
43  
44  
45  
46  
47  
48  
49  
50  
51  
52  
53  
54  
55  
56  
57  
58  
59  
60